Electronic Supplementary Material (ESI) for Journal of Materials Chemistry A.

Supplementary Information

Origin of Enhanced Oxygen Evolution Reaction Activity and Stability of Nitrogen and Cerium Co-doped CoS_2 Electrocatalyst

Jinhui Hao,[†] Wei Luo,[†] Wenshu Yang, [†] Longhua Li[†] and Weidong Shi*,[†]

[†]School of Chemistry and Chemical Engineering, Jiangsu University, Zhenjiang 212013, P. R. China

To whom correspondence should be addressed: E-mail: swd1978@ujs.edu.cn

Methods

DFT calculations. The OER process is assumed to involve four elementary reaction steps:

$$H_2O + * \rightarrow HO^* + H^+ + -e^- \quad (a)$$

$$HO^* \rightarrow O^* + H^+ + e^- \quad (b)$$

$$O^* + H_2O \rightarrow HOO^* + H^+ + e^- \quad (c)$$

$$OOH^* \rightarrow * + O_2 + H^+ + e^- \quad (d)$$

where * and *M** represent an active site and an adsorbed intermediate on the surface, respectively.

The free energy of the adsorbed state of each step was calculated as:

$$\Delta G_a = E_{(HO^*)} - E_{(*)} - E_{H_2O} + 1/2E_{H_2} + (\Delta ZPE - T\Delta S)_a - eU \quad (1)$$

$$\Delta G_b = E_{(O^*)} - E_{(HO^*)} + 1/2E_{H_2} + (\Delta ZPE - T\Delta S)_b - eU \quad (2)$$

$$\Delta G_c = E_{(HOO^*)} - E_{(O^*)} - E_{H_2O} + 1/2E_{H_2} + (\Delta ZPE - T\Delta S)_a - eU \quad (3)$$

$$\Delta G_d = E_{(*)} - E_{(HOO^*)} + E_{O_2} + 1/2E_{H_2} + (\Delta ZPE - T\Delta S)_c - eU \quad (4)$$

where $E_{(*)}$, $E_{(HO^*)}$, $E_{(O^*)}$, and $E_{(HOO^*)}$ are the energies of the pure surface and the adsorbed surfaces with HO*, O*, and HOO* , respectively. E_{H2O} and E_{H2} are the computed energies for the sole H_2O and H_2 molecules, respectively. Δ*ZPE* and Δ*S* are the zero point energy change and entropy change of intermediate adsorption. The total free energy (Δ*G*) to form one molecule of O_2 was fixed at the value of 4.92 eV. *U* (vs. RHE) is the electrode potential used for changing all the free-energy steps into downhill.

The transition state search was performing with a linear synchronous transit (LST), followed by repeated conjugate gradient minimizations and quadratic synchronous transit (QST) maximizations until a transition state has been located.

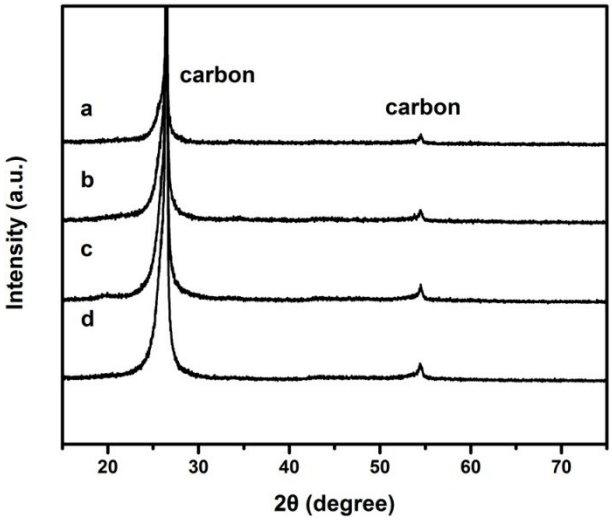

Figure S1. XRD patterns. (a) nitrate containing cerium doped precursor. (b) nitrate containing precursor. (c) cerium doped precursor. (d) pure precursor.

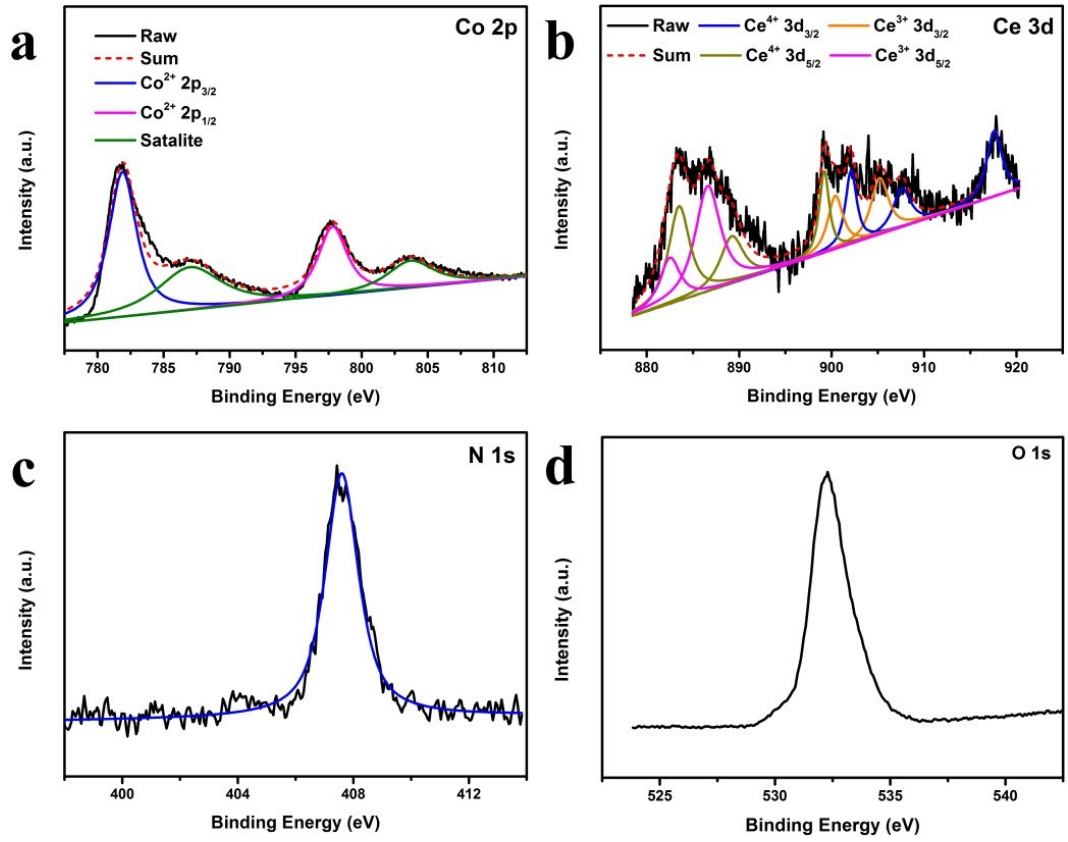

Figure S2. XPS spectra of nitrate containing cerium doped precursor. (a) Co 2p region. (b) Ce 3d region. (c) N 1s region. (d) O 1s region.

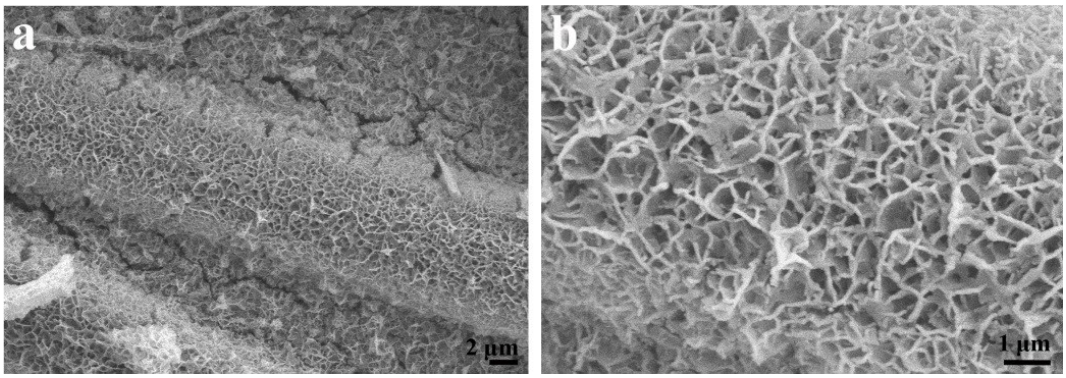

Figure S3. SEM images of nitrate containing cerium doped precursor.

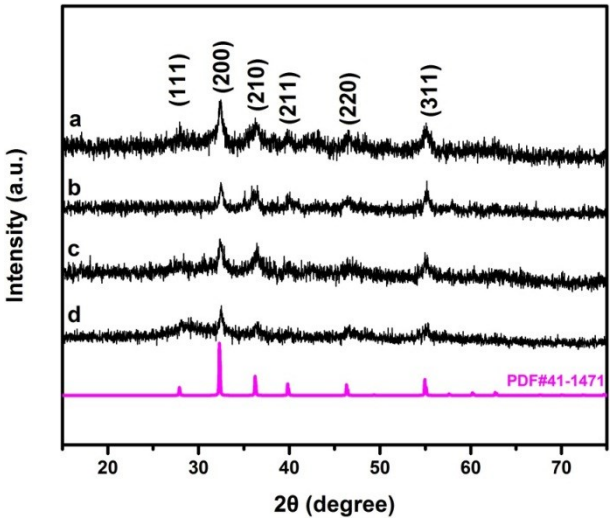

Figure S4. XRD patterns. (a) N,Ce-CoS_2. (b) N-CoS_2. (c) Ce-CoS_2. (d) CoS_2.

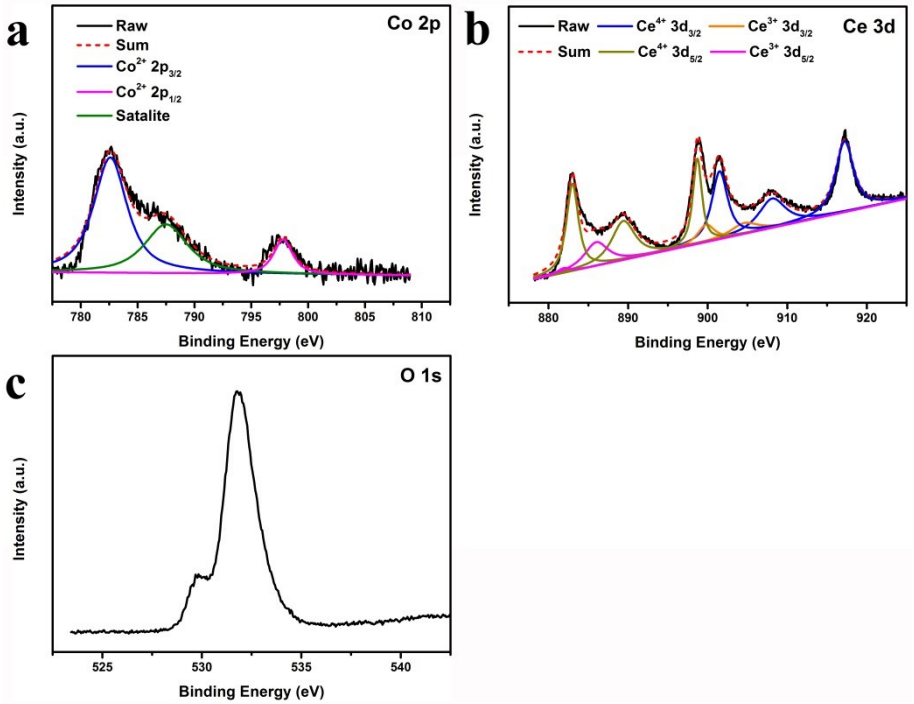

Figure S5. XPS spectra of cerium doped precursor. (a) Co 2p region. (b) Ce 3d region. (c) O 1s region.

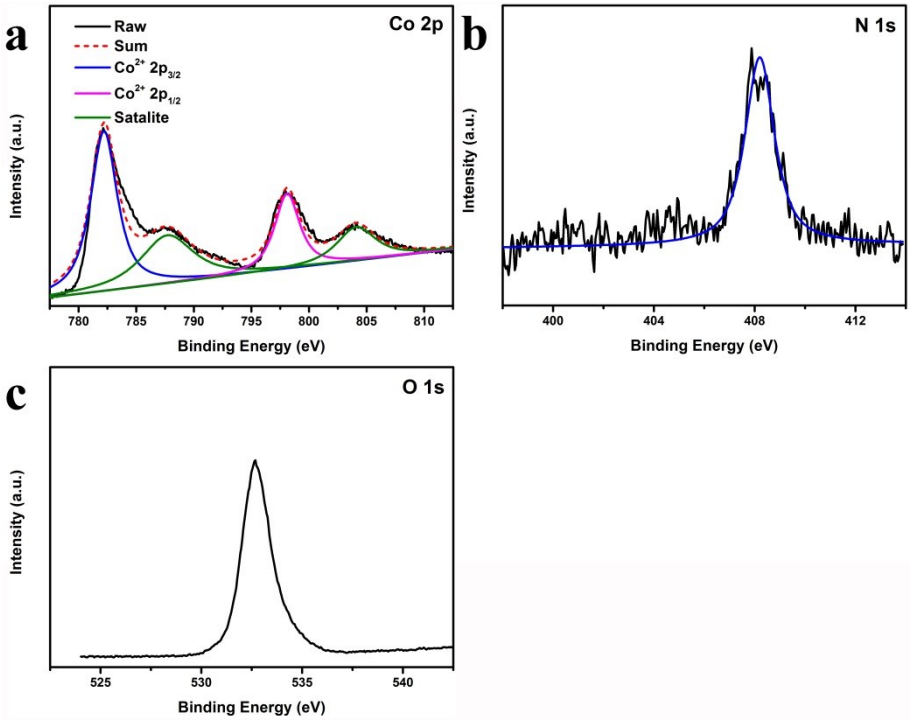

Figure S6. XPS spectra of nitrate containing precursor. (a) Co 2p region. (b) N 1s region. (c) O 1s region.

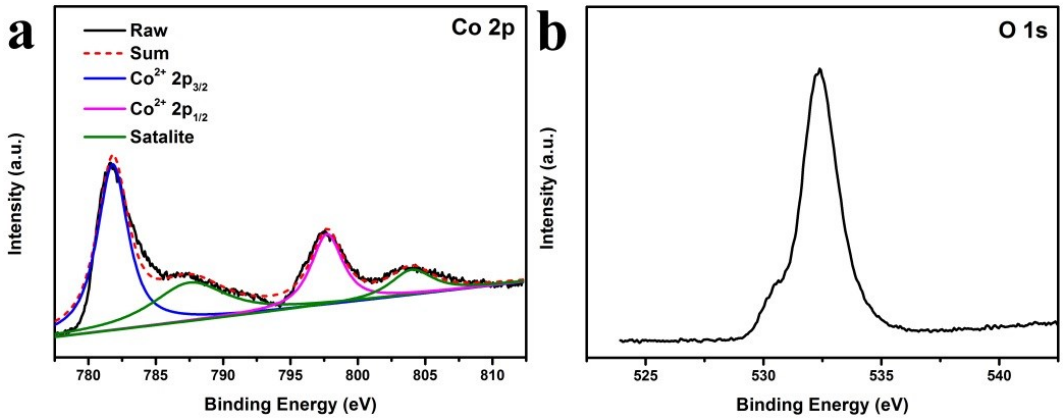

Figure S7. XPS spectra of pure precursor. (a) Co 2p region. (b) O 1s region.

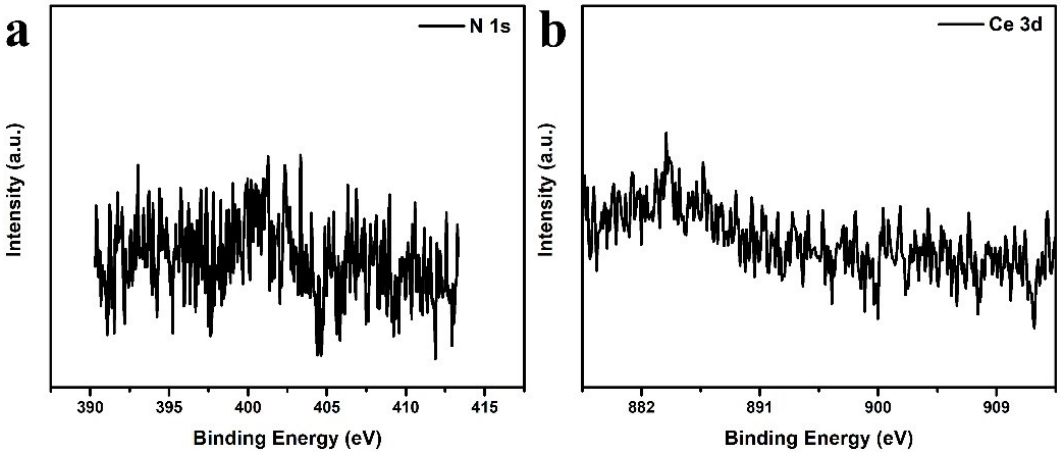

Figure S8. (a) N 1s XPS spectrum of Ce-CoS_2. (b) Ce 3d XPS spectrum of N-CoS_2.

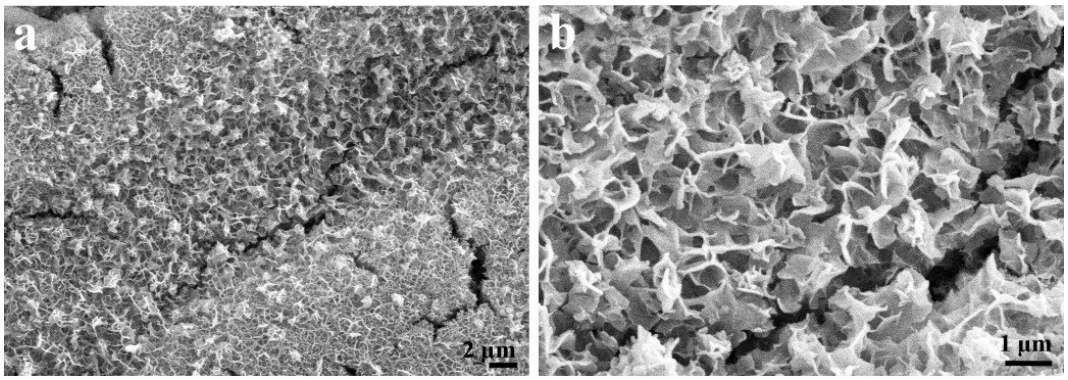

Figure S9. SEM images of N-CoS_2.

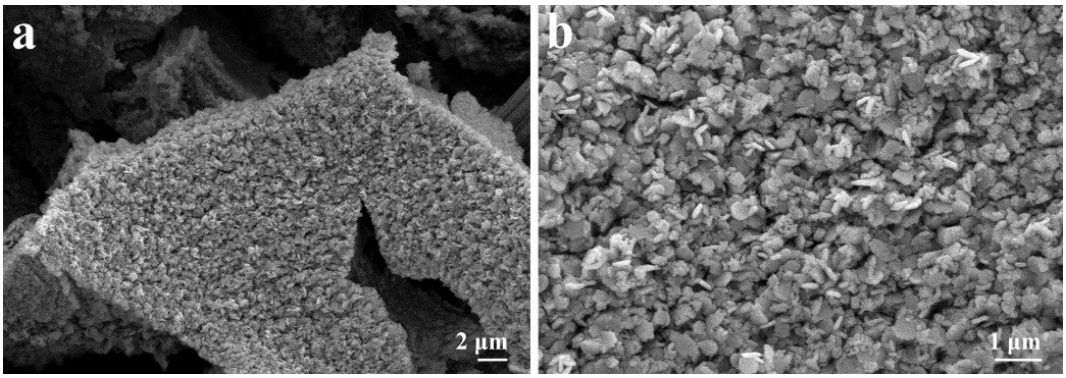

Figure S10. SEM images of Ce-CoS_2.

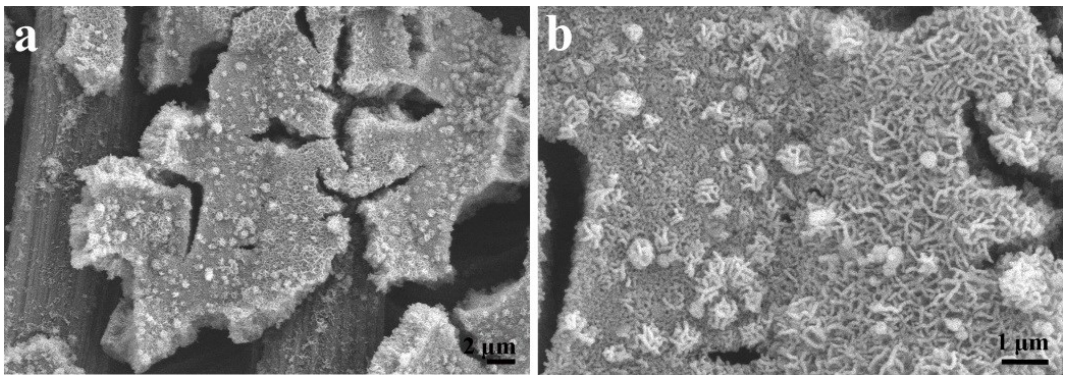

Figure S11. SEM images of CoS_2.

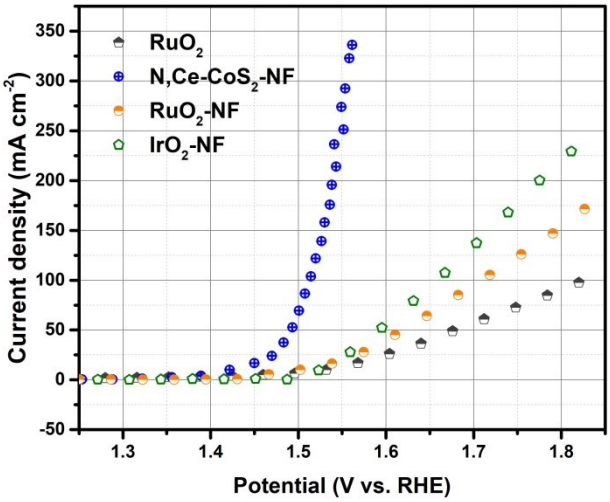

Figure S12. LSV curves of N,Ce-CoS_2-NF, RuO_2, RuO_2-NF and IrO_2-NF.

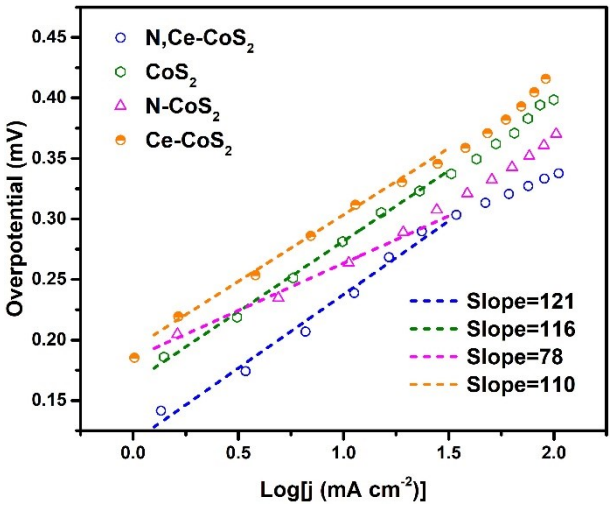

Figure S13. Tafel plots of N,Ce-CoS_2, CoS_2, N-CoS_2 and Ce-CoS_2.

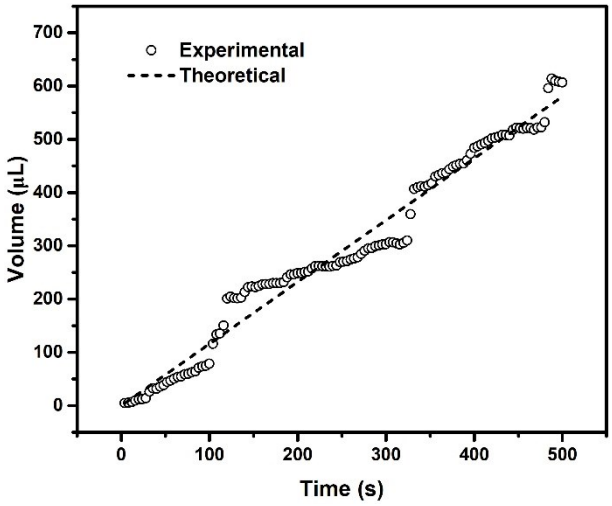

Figure S14. Faradaic efficiency on N,Ce-CoS_2 evaluated by comparing the experimental and theoretical data.

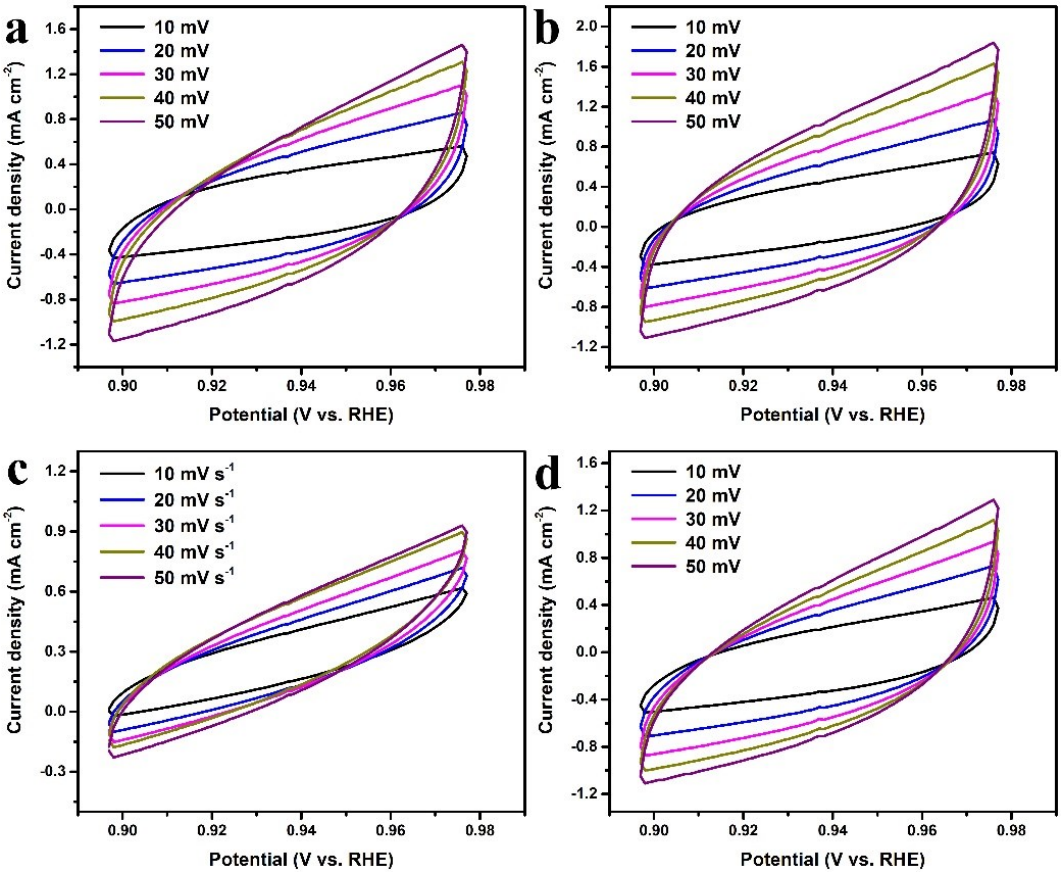

Figure S15. CV curves at different scan rates. (a) N,Ce-CoS_2. (b) N-CoS_2. (c) Ce-CoS_2. (d) CoS_2.

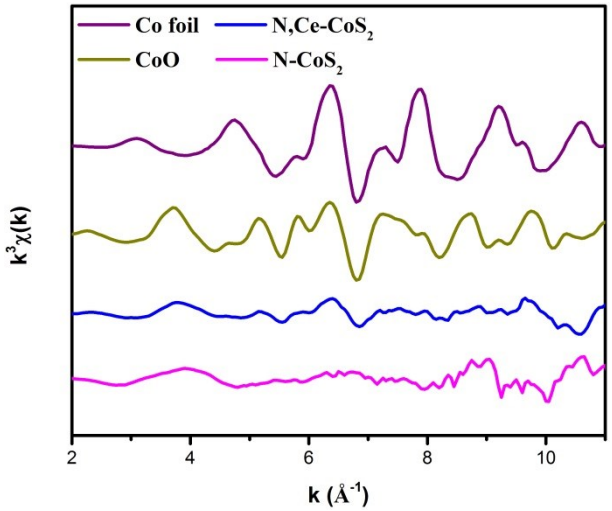

Figure S16. Co K-edge EXAFS curves in *k*-space.

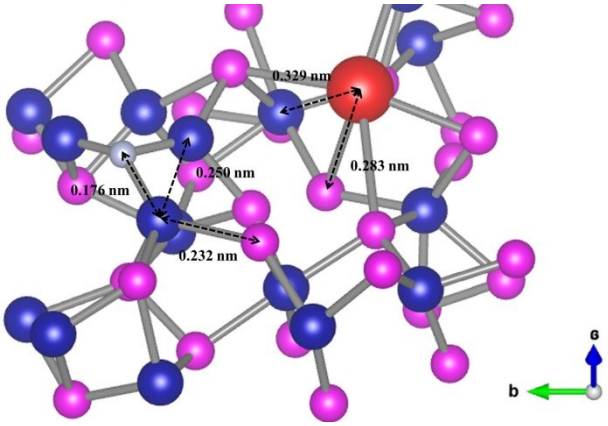

Figure S17. BL data of N,Ce-CoS_2 with optimized structure.

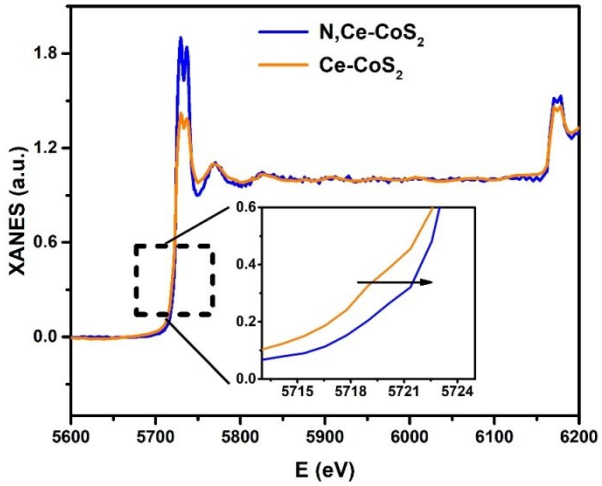

Figure S18. XANES spectra of Ce L-edge for Ce-CoS_2 and N,Ce-CoS_2. The lower right inset shows the magnified curves.

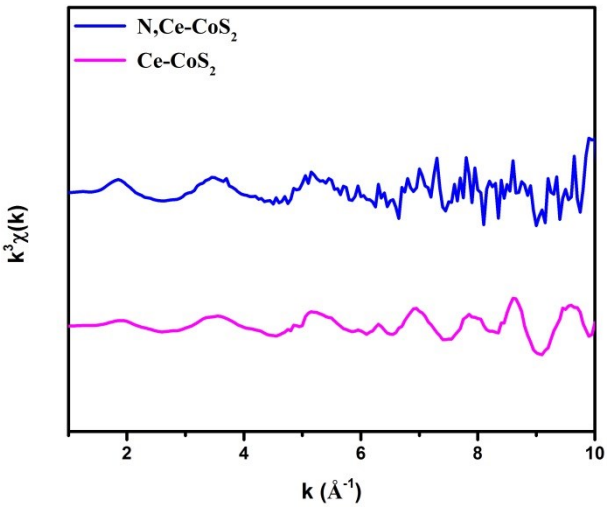

Figure S19. EXAFS curves of Ce L-edge for N,Ce-CoS_2 and Ce-CoS_2 in *k*-space.

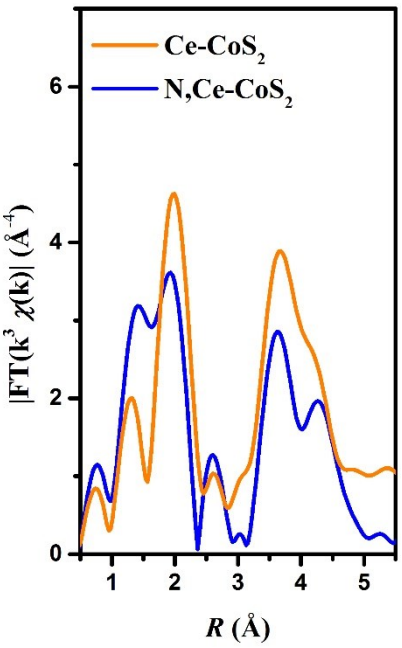

Figure S20. EXAFS-FT spectra of Ce L-edge in *R* space for Ce-CoS_2 and N,Ce-CoS_2.

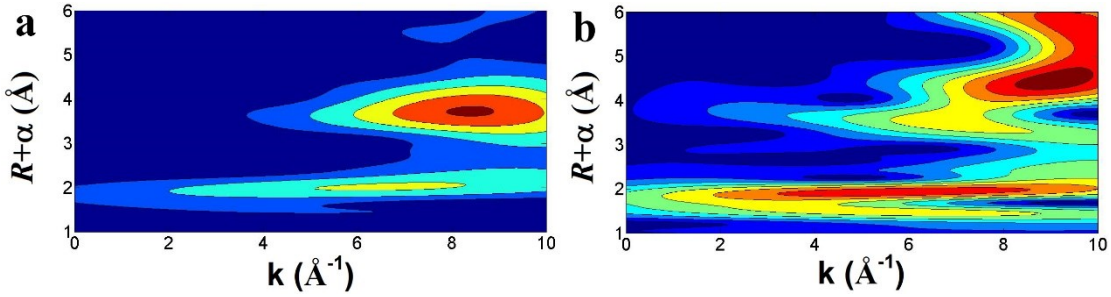

Figure S21. EXAFS-CCWT image of Ce L-edge for Ce-CoS_2 (a) and N,Ce-CoS_2 (b).

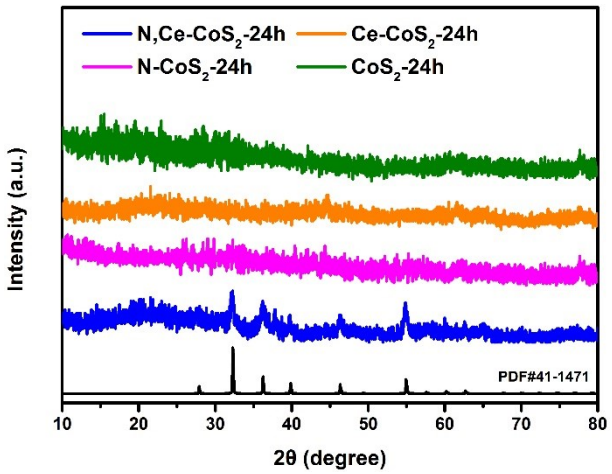

Figure S22. XRD patterns of N,Ce-CoS_2, N-CoS_2, Ce-CoS_2 and CoS_2 after 24 h OER with applied current density of 10 mA cm^{-2}.

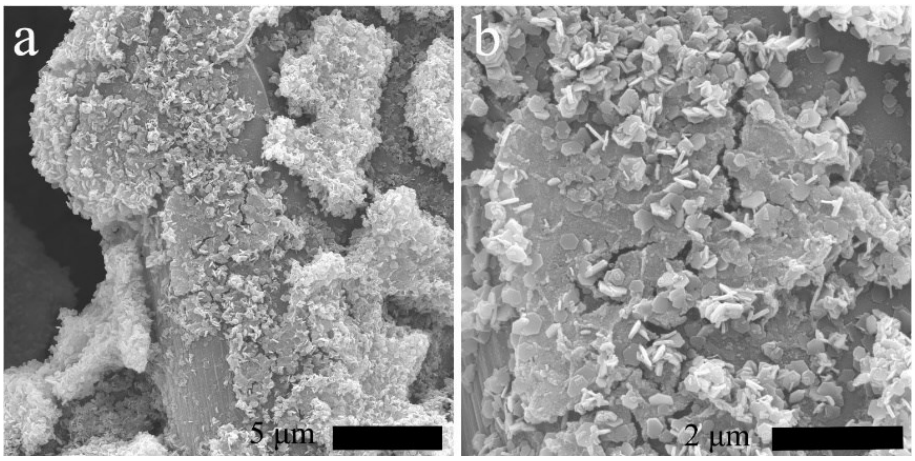

Figure S23. SEM images of N,Ce-CoS_2 after 24 h OER with applied current density of 10 mA cm^{-2}.

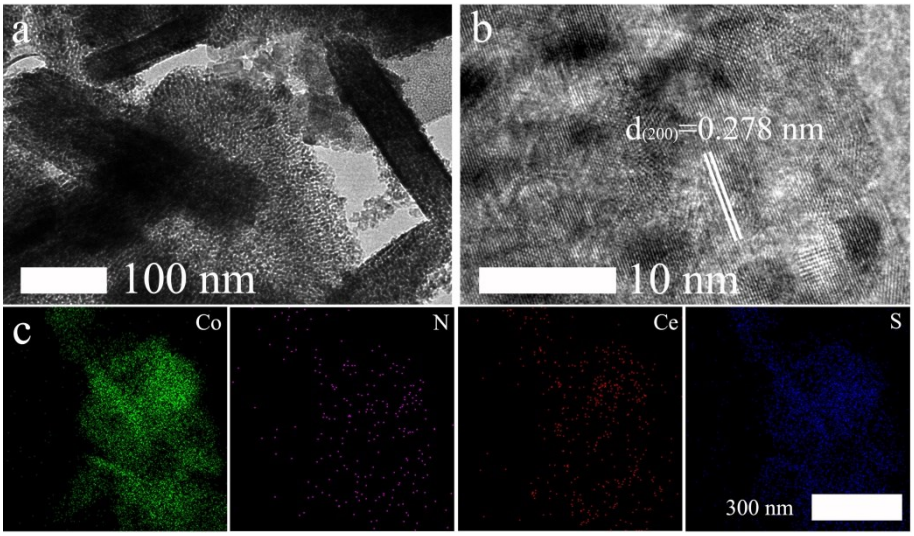

Figure S24. TEM analysis of N,Ce-CoS_2 after 24 h OER with applied current density of 10 mA cm^{-2}. (a) TEM image. (b) HRTEM image. (c) TEM-EDS elemental mapping images.

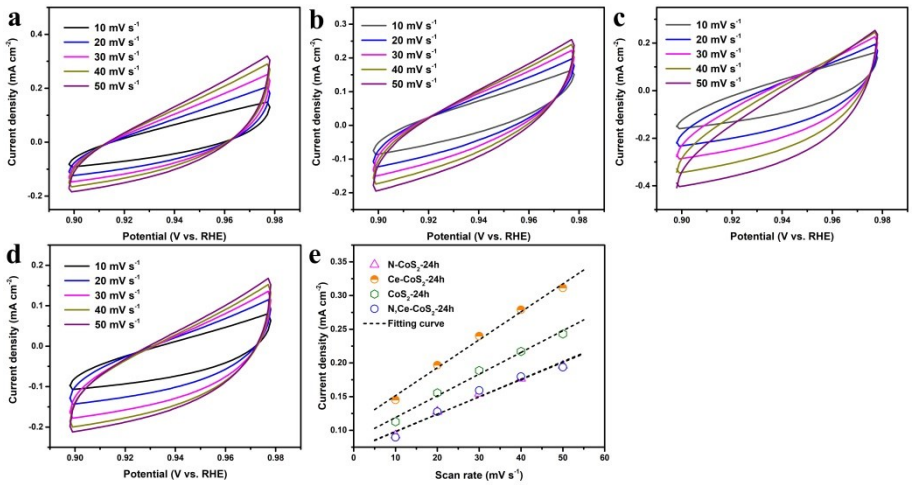

Figure S25. CV curves at different scan rates. (a) N,Ce-CoS_2-24h. (b) N-CoS_2-24h. (c) Ce-CoS_2-24h. (d) CoS_2-24h. (e) Current density differences plotted against scan rates.

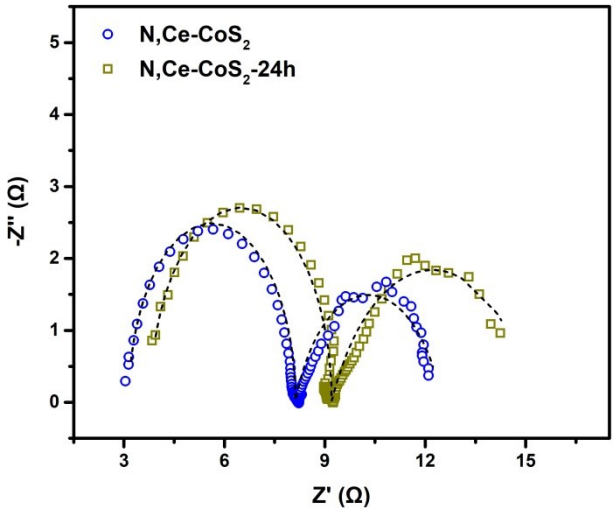

Figure S26. Nyquist plots of EIS spectra measured from N,Ce-CoS_2 and N,Ce-CoS_2-24h.

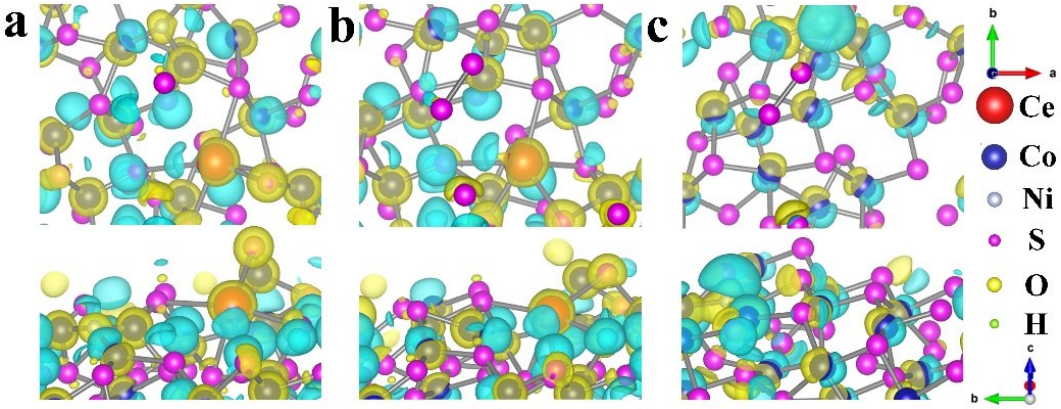

Figure S27. (a) The electron density difference map of N,Ce-CoS_2 and CoS_2. Yellow color: increased electron density; Blue green color: decreased electron density. (b) The electron density difference map of Ce-CoS_2 and CoS_2. (c) The electron density difference map of N-CoS_2 and CoS_2.

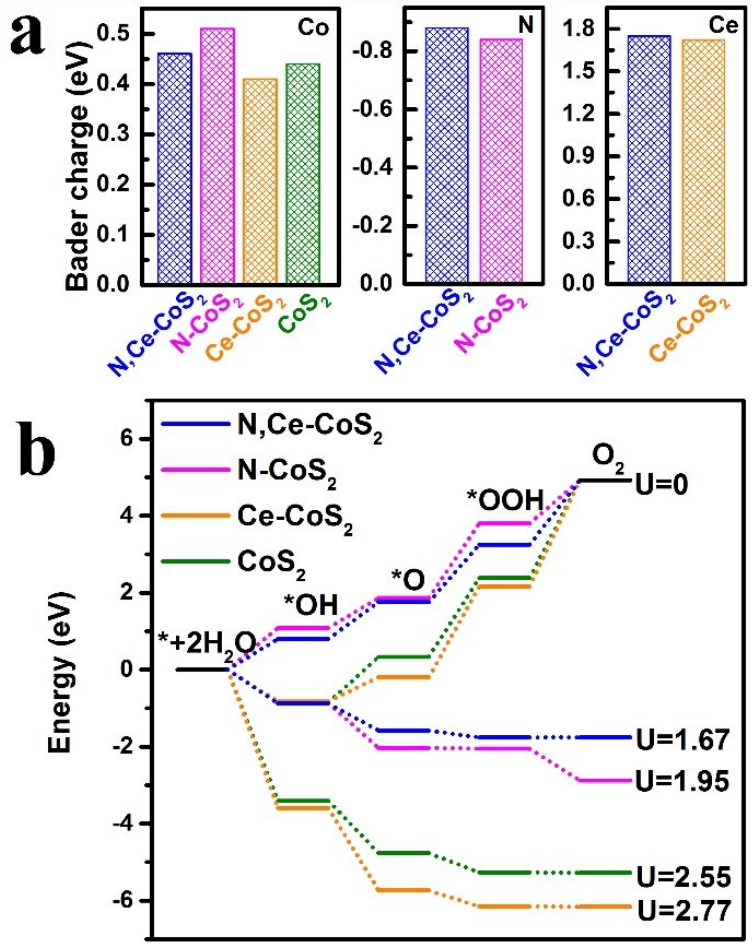

Figure S28. (a) Bader charge of Co, N and Ce atoms. (b) Calculated free energies for adsorption of intermediates with different applied potential.

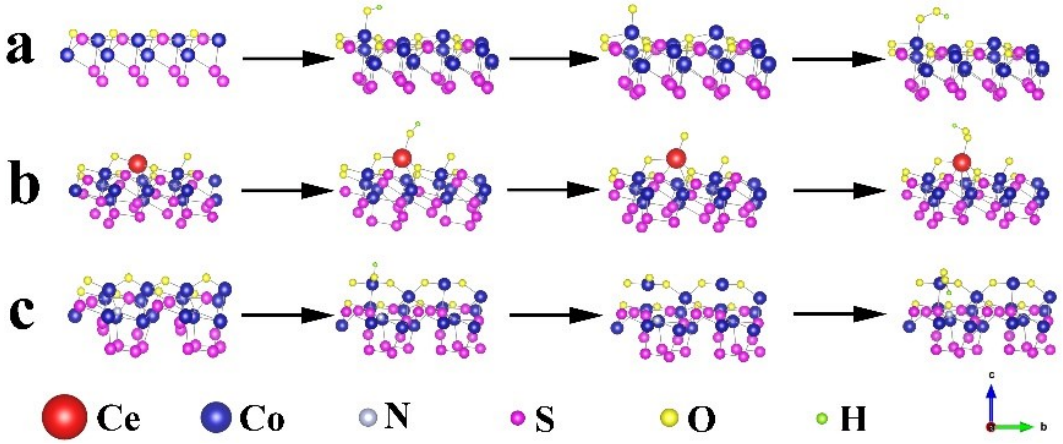

Figure S29. The reaction paths for OER on optimized electrocatalysts surfaces. (a) N-CoS_2/CoO. (b) Ce-CoS_2/CoO. (c) CoS_2/CoO.

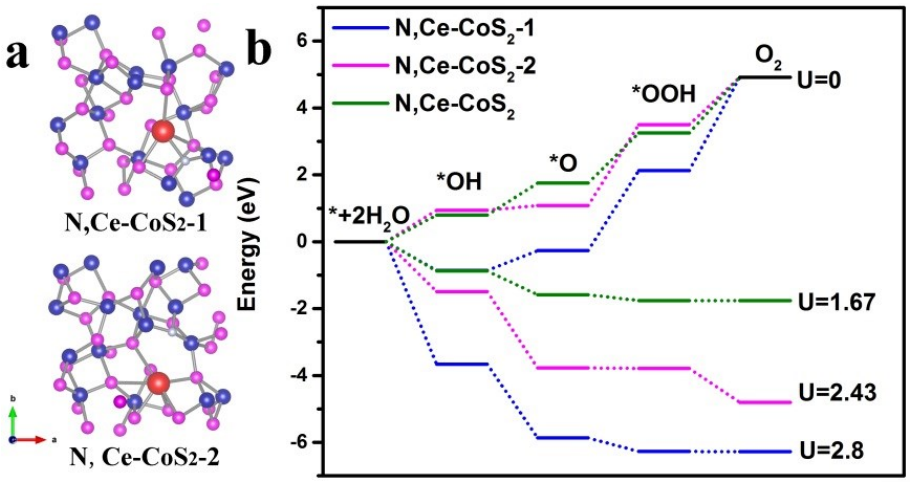

Figure S30. (a) The optimized structure of N,Ce-CoS_2-1 and N,Ce-CoS_2-2. (b) Free-energy diagram for the four steps of the OER at the different applied potentials.

.

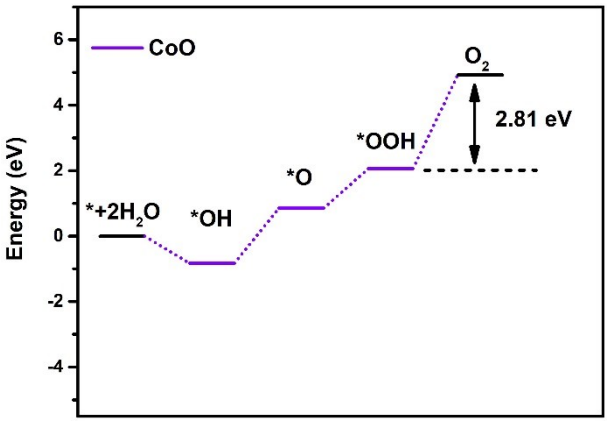

Figure S31. CoO free-energy diagram for the four steps of the OER.

Table S1. The binding energies (eV) form XPS fitting data of N,Ce-CoS_2, N-CoS_2, Ce-CoS_2 and CoS_2.

Sample	***Co^{3+} $2p_{3/2}$***	***Co^{2+} $2p_{3/2}$***	***Co^{3+} $2p_{1/2}$***	***Co^{2+} $2p_{1/2}$***	***Ce $3d_{5/2}$***	***Ce $3d_{3/2}$***
N,Ce-CoS_2	779.4	782.2	794.3	798.7	882.9 886.2	901.1 904.7
N-CoS_2	779.5	782.3	794.4	798.8	/	/
Ce-CoS_2	778.7	781.9	793.7	798.2	882.6 886.0	900.9 904.6
CoS_2	/	782.1	/	798.4	/	/

Table S2. The morphology size of N,Ce-CoS_2, N-CoS_2, Ce-CoS_2 and CoS_2.

Sample	***Length (nm)***	***Thickness (nm)***
N,Ce-CoS_2	630	110
N-CoS_2	820	70
Ce-CoS_2	400	170
CoS_2	520	130

Table S3. ICP-MS analysis of Co and Ce concentration in the acidic solution.

Sample	***Co***	***Ce***	***S***
N,Ce-CoS_2	2.92 μmol g^{-1}	0.095 μmol g^{-1}	5.84 μmol g^{-1}
N,Ce-CoS_2-24h	1.77 μg g^{-1}	0.34 μg g^{-1}	2.57 μg g^{-1}

Table S4. The mass loading of electrocatalysts on carbon paper.

Sample	N,Ce-CoS_2	N-CoS_2	Ce-CoS_2	CoS_2
Mass loading (mg)	0.47	0.49	0.44	0.52

Table S5. OER electrocatalysts and their performance.

Electrocatalyst	*Overpetential (mV) at 10 mA cm^{-2}*	*Electrolyte*	*Referencee*
N,Ce-NiS_2	220	1 M KOH	This work
N,Ce-NiS_2/Ni foam	190	1 M KOH	This work
LaNiFe(OH)/Ni foam	189	1M KOH	[1]
Co_3O_4/$Fe_{0.33}Co_{0.66}P$	<200	1M KOH	[2]
Cu@NiFe LDH/Cu foam	199	1M KOH	[3]
NiFeCu/Ni foam	180	1M KOH	[4]
NiFe/Ni foam	<200	1M KOH	[5]
NiO/NiFe LDH/ Cu foam	<200	1M KOH	[6]
MoS_2/Co_9S_8/Ni_3S_2/Ni	166	1M KOH	[7]
FeP/Ni2P/Ni foam	190	1M KOH	[8]
Fe^{2+}--NiFe LDHs/Ni foam	195	1M KOH	[9]
$Ni_xFe_{1-x}Se_2$/Ni foam	195	1M KOH	[10]
N-Co_3O_4/Ni foam	190	1M KOH	[11]
$FeNiS_2$ NS/rGO	200	1M KOH	[12]
(NiFe)OOH	<200	1M KOH	[13]
Au/$NiFeO_x$	190	1 M KOH	[14]
CoFeW cluster	192	1 M KOH	[15]
EBP@NG	191	1 M KOH	[16]
FeCoW	191	1M KOH	[17]
Ru/CoFe-LDHs	198	1 M KOH	[18]
N-$NiMoO_4$/NiS_2	283	1 M KOH	[19]
NiFe-LDH	270	1 M KOH	[20]
AN-CuNiFe	224	1 M KOH	[21]
NiFe MOFs	300	1 M KOH	[22]
Ru_1–Pt_3Cu	220	1 M KOH	[23]
W-$Ni(OH)_2$	237	1 M KOH	[24]
NiCoFe@NiCoFeO	201	1 M KOH	[25]
Pt-NC/Ni-MOF	292	1 M KOH	[26]
N-CoS_2	240	1 M KOH	[27]
N-NiS_2	270	1 M KOH	[28]
NiFe-LDH/CNTs	247	1M KOH	[29]
FeCoW/Ni foam	250	1M KOH	[30]
NiCoP/C	330	1M KOH	[31]
Co_4N	257	1M KOH	[32]
Porous MoO_2	260	1M KOH	[33]
NiFe LDH	260	1M KOH	[34]
Co-Fe-P	280	1M KOH	[35]
Co_3O_4/CNTs	290	0.1M KOH	[36]
Ni_3Se_2	290	0.3 M KOH	[37]
$NiCo_2O_4$	290	1M NaOH	[38]
CoN	290	1M KOH	[39]

Table S6. The fitting results of EIS spectra using the equivalent circuit in their inset.

Sample	R_s *(Ω)*	CPE_1 *($F \cdot cm^{-2}$)*	n_1	R_1 *(Ω)*	CPE_2 *($F \cdot cm^{-2}$)*	n_2	R_2 *(Ω)*
N,Ce-CoS_2	3.14	2.72e-7	0.99	4.98	0.22	0.76	4.37
N-CoS_2	3.64	2.23e-7	0.97	6.41	0.41	0.66	6.17
Ce-CoS_2	3.43	1.64e-7	0.99	6.72	0.28	0.79	6.14
CoS_2	4.37	2.51e-7	0.94	6.11	0.19	0.68	6.95
N,Ce-CoS_2-24h	3.79	1.68e-7	0.99	5.42	0.29	0.70	6.02

Reference

1. Gao, C. et al. An amorphous nickel-iron-based electrocatalyst with unusual local structures for ultrafast oxygen evolution reaction. *Adv. Mater.* **31**, 1900883 (2019).
2. Zhang, X. et al. $Co_3O_4/Fe_{0.33}Co_{0.66}P$ interface nanowire for enhancing water oxidation catalysis at high current density. *Adv. Mater.* **30**, 1803551 (2018).
3. Yu, L. et al. Cu nanowires shelled with NiFe layered double hydroxide nanosheets as bifunctional electrocatalysts for overall water splitting. *Energy Environ. Sci.* **10**, 1820–1827 (2017).
4. Zhang, P. et al. Dendritic core-shell nickel-iron-copper metal/metal oxide electrode for efficient electrocatalytic water oxidation. *Nat. Commun.* **9**, 381 (2018).
5. Lu, X. & Zhao, C. Electrodeposition of hierarchically structured-dimensional nickel-iron electrodes for efficient oxygen evolution at high current densities. *Nat. Commun.* **6**, 6616 (2015).
6. Gao, Z.W. et al. Engineering NiO/NiFe LDH intersection to bypass scaling relationship for oxygen evolution reaction via dynamic tridimensional adsorption of intermediates. *Adv. Mater.* **31**, 1804769 (2019).
7. Yang, Y. et al. Hierarchical nanoassembly of $MoS_2/Co_9S_8/Ni_3S_2$/Ni as a highly efficient electrocatalyst for overall water splitting in a wide pH range. *J. Am. Chem. Soc.* **141**, 10417–10430 (2019).
8. Yu, F. et al. High-performance bifunctional porous non-noble metal phosphide catalyst for overall water splitting. *Nat. Commun.* **9**, 2551 (2018).
9. Cai, Z. et al. Introducing Fe^{2+} into nickel-iron layered double hydroxide: Local structure modulated water oxidation activity. *Angew. Chem. Int. Ed.* **57**, 9392–9396 (2018).
10. Xu, X., Song, F. & Hu, X. A nickel iron diselenide-derived efficient oxygen-evolution catalyst. *Nat. Commun.* **7**, 12324 (2016).
11. Li, X. et al. Nitrogen-doped cobalt oxide nanostructures derived from cobalt-alanine complexes for high-performance oxygen evolution reactions. *Adv. Funct. Mater.* **28**, 1800886 (2018).
12. Jiang, J. et al. Ultrahigh electrocatalytic oxygen evolution by iron-nickel sulfide nanosheets/reduced graphene oxide nanohybrids with an optimized autoxidation process. *Nano Energy* **43**, 300-309 (2018).
13. Zhou, H. et al. Water splitting by electrolysis at high current densities under 1.6 volts. *Energy Environ. Sci.* **11**, 2858-2864 (2018).
14. Li, J. et al. Breathing-Mimicking Electrocatalysis for Oxygen Evolution and Reduction. Joule 3,557–569 (2019).
15. Han, X.-B. et al. Ultrasmall Abundant Metal-Based Clusters as Oxygen-Evolving Catalysts. *J. Am. Chem. Soc.* **141**, 232–239 (2019).
16. Yuan, Z. et al. Ultrathin Black Phosphorus-on-Nitrogen Doped Graphene for Efficient Overall Water Splitting: Dual Modulation Roles of Directional Interfacial Charge Transfer. *J. Am. Chem. Soc.* **141**, 4972–4979 (2019).
17. Zhang, B. et al. Homogeneously dispersed, multimetal oxygen-evolving catalysts. *Science* **352**, 333–337 (2016).
18. Li, P. et al. Boosting oxygen evolution of single-atomic ruthenium through electronic coupling with cobalt-iron layered double hydroxides. *Nat. Commun.* **10**, 1711 (2019).

19. An, L. et al. Epitaxial Heterogeneous Interfaces on N-$NiMoO_4$/NiS_2 Nanowires/Nanosheets to Boost Hydrogen and Oxygen Production for Overall Water Splitting. *Adv. Funct. Mater.* **29**, 1805298 (2019).
20. Zhou, D. et al. NiFe Hydroxide Lattice Tensile Strain: Enhancement of Adsorption of Oxygenated Intermediates for Efficient Water Oxidation Catalysis. *Angew. Chem. Int. Ed.* **58**, 736–740 (2019).
21. Cai, Z. et al. Amorphous Nanocages of Cu-Ni-Fe Hydr(oxy)oxide Prepared by Photocorrosion For Highly Efficient Oxygen Evolution. *Angew. Chem. Int. Ed.* **58**, 4189–4194 (2019).
22. Cheng, W. et al. Lattice-strained metal–organic-framework arrays for bifunctional oxygen electrocatalysis. *Nat. Energy* **4**, 115–122 (2019).
23. Yao, Y. et al. Engineering the electronic structure of single atom Ru sites via compressive strain boosts acidic water oxidation electrocatalysis. *Nat. Catal.* **2**, 304–313 (2019).
24. Yan, J. et al. Single atom tungsten doped ultrathin α-$Ni(OH)_2$ for enhanced electrocatalytic water oxidation. *Nat. Commun.* **10**, 2149 (2019).
25. Liu, Y. et al. Valence Engineering via Selective Atomic Substitution on Tetrahedral Sites in Spinel Oxide for Highly Enhanced Oxygen Evolution Catalysis. *J. Am. Chem. Soc.* **141**, 8136–8145 (2019).
26. Guo, C. et al. Intermediate Modulation on Noble Metal Hybridized to 2D Metal-Organic Framework for Accelerated Water Electrocatalysis. *Chem*, 1–13 (2019).
27. Hao, J. et al. A Nitrogen Doping Method for CoS_2 Electrocatalysts with Enhanced Water Oxidation Performance. *ACS Catal.* **7**, 4214–4220 (2017).
28. Hao, J. et al. Nitrogen Doped NiS_2 Nanoarray with Enhanced Electrocatalytic Activity for Water Oxidation. *J. Mater. Chem. A* **5**, 17811–17816 (2017).
29. Gong, M. et al. An Advanced Ni–Fe Layered Double Hydroxide Electrocatalyst for Water Oxidation. *J. Am. Chem. Soc.* **135**, 8452–8455 (2013).
30. Pi, Y. et al. Trimetallic Oxyhydroxide Coralloids for Efficient Oxygen Evolution Electrocatalysis. *Angew. Chem.* **129**, 4573–4577 (2017).
31. He, P., Yu, X.-Y. & Lou, X.W. Carbon-Incorporated Nickel–Cobalt Mixed Metal Phosphide Nanoboxes with Enhanced Electrocatalytic Activity for Oxygen Evolution. *Angew. Chem.* **129**, 3955–3958 (2017).
32. Chen, P. et al. Metallic Co_4N Porous Nanowire Arrays Activated by Surface Oxidation as Electrocatalysts for the Oxygen Evolution Reaction. *Angew. Chem.* **127**, 14923–14927 (2015).
33. Jin, Y. et al. Porous MoO_2 Nanosheets as Non-noble Bifunctional Electrocatalysts for Overall Water Splitting. *Adv. Mater.* **28**, 3785–3790 (2016).
34. Hunter, B.M. et al. Highly Active Mixed-Metal Nanosheet Water Oxidation Catalysts Made by Pulsed-Laser Ablation in Liquids. *J. Am. Chem. Soc.* **136**, 13118–13121 (2014).
35. Mendoza-Garcia, A. et al. Controlled Anisotropic Growth of Co-Fe-P from Co-Fe-O Nanoparticles. *Angew. Chem. Int. Ed.* **54**, 9642–9645 (2015).
36. Ma, T.Y., Dai, S., Jaroniec, M. & Qiao, S.Z. Metal–Organic Framework Derived Hybrid Co3O4-Carbon Porous Nanowire Arrays as Reversible Oxygen Evolution Electrodes. *J. Am. Chem. Soc.* **136**, 13925–13931 (2014).
37. Swesi, A.T., Masud, J. & Nath, M. Nickel selenide as a high-efficiency catalyst for oxygen evolution reaction. *Energy Environ. Sci.* **9**, 1771–1782 (2016).
38. Gao, X. et al. Hierarchical $NiCo_2O_4$ Hollow Microcuboids as Bifunctional Electrocatalysts for

Overall Water-Splitting. *Angew. Chem. Int. Ed.* **55**, 6290–6294 (2016).

39. Zhang, Y. et al. Rapid Synthesis of Cobalt Nitride Nanowires: Highly Efficient and Low-Cost Catalysts for Oxygen Evolution. *Angew. Chem. Int. Ed.* **55**, 8670–8674 (2016).